

Oxidation Behavior of the Polycrystalline Ni-Base Superalloy VDM® Alloy 780



A. KIRCHMAYER, M. WEISER , P. RANDELZHOFFER, L.P. FREUND, B. GEHRMANN, M. HAFEZ HAGHIGHAT, D. HUENERT, M. GÖKEN, and S. NEUMEIER

VDM® Alloy 780 is a newly developed polycrystalline Ni-base superalloy with high contents of Co, Cr, and Al intended for operating temperatures up to 750 °C. The alloy is precipitation strengthened by the γ' phase, which is analyzed by atom probe tomography. Additionally, δ and η phases are utilized for grain boundary pinning. It is shown that the δ and η phases precipitate either plate like or in a fine lamellar structure inside each other. VDM® Alloy 780 shows superior oxidation resistance in comparison with Udimet 720Li and A718Plus, as seen by a lower mass gain and thinner oxide layers at 800 °C and 900 °C. This superior behavior is analyzed in detail by TEM and STEM investigations of the oxide scales from which it is concluded that the Al/Ti ratio in these alloys plays an important role on the oxidation behavior.

<https://doi.org/10.1007/s11661-022-06956-z>
© The Author(s) 2023

I. INTRODUCTION

POLYCRYSTALLINE Ni-base superalloys are essential for high-temperature applications in aggressive environments as they are present in stationary gas turbines or aeroplane engines. Superalloys exhibit high strength, good creep properties, and sufficient oxidation and corrosion resistance at high temperatures.^[1] This is challenging, since the atmospheres inside the turbines vary, especially when different fuels are used and the possible usage of hydrogen becomes increasingly important.^[2] To improve the environmental-friendliness of these turbines, new Ni-base superalloys are in development, which should have better mechanical and

chemical properties compared to commercially used alloys at higher service temperatures. One of these newly developed alloys is the VDM® Alloy 780 (hereinafter called VDM Alloy 780). VDM Alloy 780 is a γ' hardened Ni-base superalloy similar to Allvac718Plus (hence called A718Plus), with a higher Co and Al content and a lower Ni and Fe content to have a sufficiently low γ' solvus temperature at a simultaneously high γ' volume fraction.^[3] Furthermore, the higher Co content leads to a higher volume fraction of the orthorhombic D0_a (Ni₃Nb) δ and the hexagonal D0₂₄ (Ni₃Ti or Ni₆AlNb) η phase,^[3] which act as grain boundary pinning phases. Both phases exhibit high solvus temperatures (970 °C to 1026 °C for δ ^[4,5] and 970 °C to 1010 °C for η ^[5]) and prevents the formation of γ'' .^[3] The fine grained microstructure is stable even after long exposures at high temperatures.^[6] Additionally, the Ti content is reduced compared to A718Plus, to achieve a high Al/Ti ratio of about 12.6 (at. pct). This Al/Ti ratio benefits the precipitation of the η phase, as Al and Ti are known to accumulate in the η phase.^[5,7] This enables a fine grained structure at elevated temperatures with a simultaneous good forgeability.^[6,8–11] High-resolution transmission electron microscopy (HRTEM) and atom probe tomography (APT) investigations of VDM Alloy 780 and A718Plus have shown that δ and η phases precipitate inside each other in a fine lamellar structure with only a few nanometers thickness.^[7,9,12] This makes the differentiation of the δ and η phase very difficult and requires advanced characterization methods. Additionally, these phases can alter the oxidation behavior of the alloy.^[13]

A. KIRCHMAYER, M. WEISER, M. GÖKEN, and S. NEUMEIER are with the Department of Materials Science & Engineering, Institute I, Friedrich-Alexander-Universität Erlangen-Nürnberg, Martensstraße 5, 91058 Erlangen, Germany. Contact e-mail: andreas.kirchmayer@fau.de P. RANDELZHOFFER is with the Department of Materials Science & Engineering, Institute II, Friedrich-Alexander-Universität Erlangen-Nürnberg, Martensstraße 5, 91058 Erlangen, Germany. L.P. FREUND is with the Department of Materials Science & Engineering, Institute I, Friedrich-Alexander-Universität Erlangen-Nürnberg and also with the MTU Aero Engine AG, Dachauer Straße 665, 80995 München, Germany. B. GEHRMANN and M. HAFEZ HAGHIGHAT are with the VDM Metals International GmbH, Kleffstraße 23, 58762 Altena, Germany. D. HUENERT is with the Projektträger Jülich, Forschungszentrum Jülich GmbH, Zimmerstraße 26-27, 10969 Berlin, Germany.

Manuscript submitted September 5, 2022; accepted December 28, 2022.

Article published online January 21, 2023

Ni-base superalloys with a relatively high content of Al and Cr, like A718Plus, are known for their good high-temperature oxidation resistance due to the formation of stable, continuous layers of Al₂O₃ and Cr₂O₃,^[13] which effectively slow down diffusional transport and reduce further oxidation.^[1,14–17] In Ni-base alloys, higher temperature facilitates the formation of continuous Al₂O₃ layers.^[14,18]

To get an insight into the different strength-increasing precipitate phases, a detailed analysis of the different precipitates of VDM Alloy 780 was conducted in this study by means of scanning electron microscope (SEM), scanning transmission electron microscopy (STEM), and atom probe tomography (APT), with focus on the δ and η morphology as well as the composition of γ' and the surrounding matrix. Additionally, the high-temperature oxidation resistance of VDM Alloy 780 at different temperatures in dry and humid atmosphere is investigated. The gained insight is correlated with a detailed analysis of the microstructural and chemical composition of the different oxide layers as well as the microstructural features of the alloy such as the δ and the η phase. These results are compared to the performance of commercially used Ni-base superalloys A718Plus and Udimet 720Li.

II. EXPERIMENTAL METHODS

The composition of the materials used in this study are shown in Table I.

The VDM Alloy 780 was heat treated as follows: 900 °C/11 h + 955 °C/1 h + 800 °C/8 h + 650 °C/8 h. A718Plus and Udimet 720Li were subjected to standard heat treatments (SHT) accordingly.^[20,21]

For thermal exposures and interrupted mass gain measurements, plates of each alloy were manually ground (final grit size: 1200) and ultrasonically cleaned in ethanol and acetone. Oxidation experiments were conducted at 800 °C for 500 h and 900 °C for 125 h in dry and humid atmosphere each. The three materials were simultaneously oxidized using a horizontal tube furnace (Carbolite/Gero; EHA12/450B). The flow rate of the gases was set to 12 l/h through a 50 mm tube diameter. The dry atmosphere was composed of synthetic air, oxygen (20 ± 2 vol pct) and nitrogen (bal.) with a water content of less than 2 vol pct. For the humid atmosphere, the synthetic air was directed through a water-filled washing bottle to achieve a humidity of 45 pct. The mass gain was measured using an analysis scale (Kern; ABT220-5DM).

APT measurements were performed on a CAMECA LEAP 4000X HR using laser mode with a laser intensity of 70 pJ, a pulse rate of 200 kHz, and a temperature of 55 K. The targeted sample preparation by a lift-out method in a Zeiss Crossbeam 540 followed conventional protocols as described in References 22, 23. Data processing was done using the commercial software IVAS 3.6.8 by Cameca and was supported by further analysis in a Matlab data analysis toolbox.

The microstructural analyses were done using the Zeiss Crossbeam 540 SEM in backscattered mode (BSE) mode with an acceleration voltage of 20 kV at a working distance of 8.5 mm. The same parameters were used for energy-dispersive X-ray spectroscopy (EDX). Scanning transmission electron microscopy (STEM) used the same setup with an acceleration voltage of 30 kV at a working distance of 2 mm. The oxide layer thickness as well as the grain size was determined using ImageJ.^[24] To reduce spallation of the oxide scale during the preparation of cross-sections, oxidized samples were electrochemically coated by a Ni protection layer. Sputtering of a thin Au layer was necessary to achieve sufficient conductivity of the oxidized surface prior to electrochemical deposition ($i = 20 \text{ nA/cm}^2$) in supersaturated NiSO₄ solution. For the SEM and EDX sample preparation, the samples were cut, ground, polished to 1 μm , and afterward fine polished with a colloidal silica suspension (Struers). Preparation of STEM samples proceeded *via* two different routes. For the investigation of the oxide scales, a lamella was lifted-out in a focused ion beam (FIB) from the bulk material and was further thinned to electron transparency. FIB-based target preparation was conducted in an FEI Helios NanoLab 600i. For the precipitate analysis, the samples were cut and ground to a thickness of 100 μm . These thin plates were further thinned using a two-component electrolyte (Tenupol 5; Struers) with a current of 50 V at – 25 °C. A Philips CM200 transmission electron microscope was used with an acceleration voltage of 200 kV for microstructural and EDX measurements.

III. RESULTS

A. Microstructural Analysis

The microstructure of VDM Alloy 780 is shown in Figure 1. Beside the γ matrix, three different phases can be distinguished using the BSD contrast (Figure 1(a)). The γ' precipitates are visible as cubic precipitates with a

Table I. Nominal Composition of VDM Alloy 780, A718Plus, and Udimet 720Li in wt pct^[19–21]

	Ni	Co	Cr	Nb	Al	Ti	Mo	Fe	W
VDM Alloy 780	bal.	25.0	18.0	5.4	2.0	0.3	3.0	< 3.0	—
A718Plus	bal.	8.0–10.0	17.0–21.0	5.2–5.8	1.2–1.7	0.5–1.0	2.5–3.1	8.0–10.0	0.8–1.4
Udimet 720Li	bal.	14.0–15.5	15.5–16.5	—	2.25–2.75	4.75–5.25	2.75–3.25	—	1.0–1.5

Note that the concentrations of the minor elements like C and B are not listed although they are present in all investigated alloys.

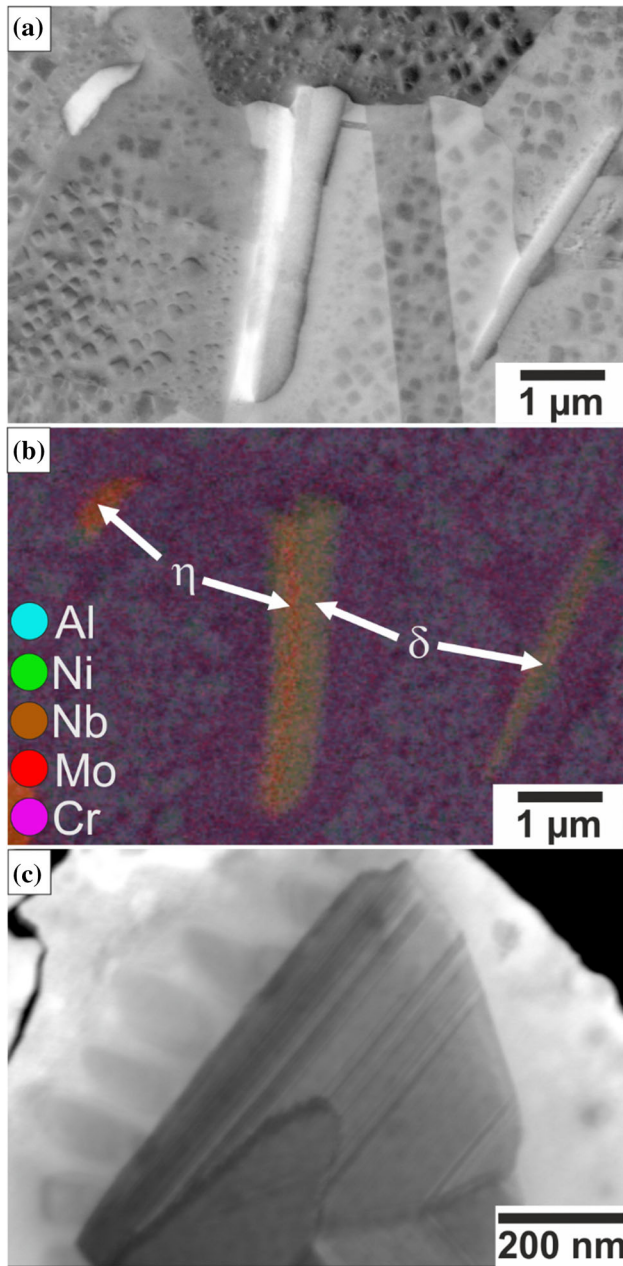


Fig. 1—Microstructure of VDM Alloy 780: (a) BSD image of coarse blocky δ (bright) and η (dark) precipitates next to each other with (b) the corresponding EDX measurement. (c) STEM bright field image of thin alternating lamella of δ (bright) and η (dark) precipitates.

dark BSD contrast and an average diameter of 110 nm and an area fraction of 28 pct. The cubic γ' shape is a result of the large positive γ/γ' lattice misfit of 0.48 pct.^[25] The δ and η phases can either precipitate isolated or beside each other as shown in Figure 1(a), where δ shows a bright BSD contrast in comparison with the slightly darker η phase. Similar arrangements of the δ and η phases were also observed in another study on VDM Alloy 780^[9] and in the similar alloy A718Plus,^[5,26] Hausmann *et al.* could reveal that the type of phase which forms and the arrangement of phases with similar compositions depends strongly on the previous

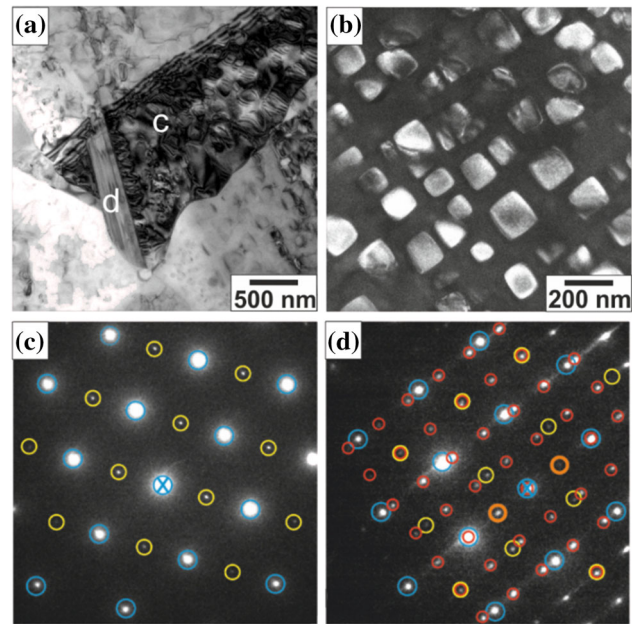


Fig. 2—TEM (a) bright field image of blocky, lamellar δ and η surrounded by γ' (b) dark field image of γ' . (c) and (d) Diffraction patterns of the areas marked in (a). Blue, yellow, red, and orange circles indicate reflections of the γ , γ' , δ and η phase accordingly (Color figure online).

thermomechanical processing steps and the resulting local chemical compositions.^[7] It is notable that the size of the γ' precipitates alters in the surrounding of the δ and η phase. EDX measurements of the blocky precipitates (Figure 1(b)) reveal that both phases show an enrichment of Ni, Nb, Ti, and Mo with an additional enrichment of Al in the δ phase. Notable is the enrichment of Mo, especially in the η phase, as this is not expected for the δ and η phase but has been detected in VDM Alloy 780 in different studies before.^[9,25] In difference to the blocky morphology, the δ and η phases can also precipitate in a fine lamellar structure (Figure 1(c)). In this case, the differentiation between the individual phases is difficult. A TEM analysis clearly reveals δ and η precipitated inside each other (Figure 2(a)) as well as cubic γ' precipitates (Figure 2(b)). With the help of the diffraction pattern and simulated phase patterns for δ and η from Reference 12, the two bright phases can be identified as δ and η . This is in agreement with the results from other works.^[9,25]

To analyze the γ/γ' microstructure in VDM Alloy 780 in more detail, an APT measurement was conducted and is shown in Figure 3. The measurement shows secondary and tertiary γ' indicated by the Al (8 at. pct) and Nb (4.4 at. pct) isosurface separated by a γ' free zone around the secondary γ' precipitates. The γ matrix is enriched in Cr and Co, as can be seen in the isosurfaces (20 at. pct each). From the displayed three-dimensional reconstruction, the chemical compositions of the secondary and tertiary γ' phase as well as the composition of the γ matrix in the γ' -free zone next to secondary γ' precipitates and within the tertiary γ' precipitates can be

extracted (Table II). The γ' phase shows an enrichment in Al and Nb, as seen in Figures 3(b) and (c) accordingly, as well as a higher content of Ni and Ti, while Cr, Co, Mo, and Fe are depleted compared to the γ matrix.

A clear depletion of Ni, Al, and Nb around the secondary γ' is found, which are typical γ' -forming elements. The precipitate-free γ matrix zone reaches 28 nm into the matrix. The composition of the γ phase between the tertiary γ' is slightly richer in γ' -forming elements. Interestingly, the composition of the matrix phase is very similar to that of medium entropy CoNiCr alloys, which are currently in focus of materials' research, see for example.^[27]

B. Oxidation Behavior

Mass gain measurements (Figure 4) point to a significantly better oxidation resistance of VDM Alloy 780 compared to Udimet 720Li and A718Plus that itself demonstrates slow oxidation rates. It is also notable that VDM Alloy 780 shows no apparent difference between dry and humid atmosphere. In contrast, this alteration of atmospheres results in a slight difference of mass gain for A718Plus and Udimet 720Li at both considered temperatures.

From the mass gain measurements, the values for the parabolic rate constants (k_w) are approximated by the linear fit of the squared mass gain over time. The results

are shown in Table III. Note that no rate constant is given for Udimet 720Li after oxidation at 900 °C in dry atmosphere, because the parabolic growth rate appears to change during oxide layer growth.

Representative BSD images of VDM Alloy 780, A718Plus, and Udimet 720Li after different exposures demonstrate multiple oxide layers distinguishable by differences in contrast (Figure 5). It has to be noted that the oxide layers of VDM Alloy 780 are identical in humid and dry air. Internal oxidation is visible in all samples. The growth of connected internal oxide phases is accompanied by a depletion of γ' in the adjacent regions. No visible microstructural differences between the samples oxidized in dry and humid atmosphere could be detected. The outer oxide layers on the VDM 780 Alloy specimens are composed of several oxide phases with considerably different contrasts in the BSD micrographs. A grain size analysis using the line interception method showed no change in grain size between oxidation at 800 °C and 900 °C in humid or dry atmosphere in all samples. VDM Alloy 780 showed an average grain size of about 3 μm , while A718Plus and Udimet 720Li have an average grain size in the range of 6 to 8 μm .

VDM 780 shows already at 800 °C for 500 h the superior oxidation resistance. Figures 5(a) and (b) show protective scale regions with a thickness of 0.3 μm for dry and humid air. Below the outer oxide layer, dark-appearing discrete oxide precipitates can be recognized in Figure 5(a). The total thickness can be approximated by 2.2 μm . The exposure at 800 °C also leads to the growth of discrete internal oxides. After an exposure at 900 °C for 125 h in dry and humid air, the entire surface is covered by a diffusion-limiting protective oxide scale, as seen in Figure 5(d). Occasionally, the protective properties of the oxide scale did not sustain among the whole surface. As shown in the micrograph of Figure 5(c), surface regions with thin (0.3 μm) dark layers are interrupted by sections that are covered with thicker multilayered oxide scales. Below the faster growing outer scale, connected oxide phases formed in the alloy. Interestingly, the resistance against oxidation does not decrease drastically during exposure at higher temperature. Samples oxidized at 800 °C exhibit a predominant thicker multiscale oxide, which is interrupted by short thinner oxide scale sections. Samples oxidized at 900 °C show an inverted behavior, there the thinner oxide is dominant and interrupted by small areas of thicker multiscale oxide. It has to be noted that the samples oxidized at 900 °C were exposed for a shorter time, so the thicker sections of the oxide scales

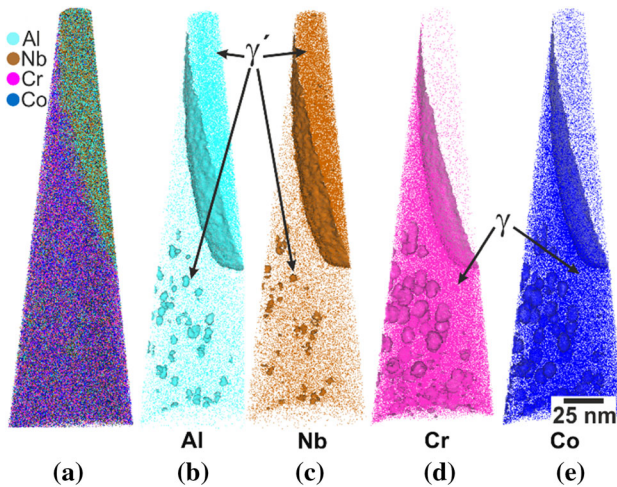


Fig. 3.—3D map generated from APT data of a γ/γ' region displaying (a) selected elements (Al: bright blue, Nb: orange, Cr: pink, Co: dark blue) and a (b) 8 at. pct Al, (c) 4.5 at. pct Nb, (d) 20 at. pct Cr and (e) 20 at. pct Co isosurface threshold (Color figure online).

Table II. Composition of Secondary γ' , the Precipitate-Free γ Matrix Zone and the γ Matrix Measured Between the Tertiary Particles in at. pct

	Ni	Co	Cr	Al	Ti	Mo	Nb	Fe
Secondary γ'	59.6	10.4	1.9	13.2	1.4	0.6	7.1	0.3
γ Matrix (γ' Free Zone)	36.1	30.6	28.4	1.1	0.1	1.4	1.1	1.2
γ Matrix	38.3	29.7	27.9	1.3	0.2	1.6	1.2	1.2

might grow more pronounced with longer exposure time.

In A718Plus (Figures 5(e) and (f)), a more homogeneous but comparably thick oxide layer is visible in all specimens. The internally grown oxides appear to follow the precipitate–matrix interface of the δ and η phase. Udimet 720Li shows a notably thicker oxide layer

compared to VDM Alloy 780 and A718Plus. The outer scale regions on Udimet 720Li reveal a considerable degree of porosity and the internal oxide phases penetrated deeper into the bulk material.

The average thickness of all oxide layers as well as the γ' depletion zone beneath the oxide scales per sample is summarized in Figure 6. It can be seen that the thinner oxide layer of the VDM Alloy 780 correlates with a larger γ' depletion zone. This is especially pronounced after the oxidation at 900 °C, as VDM Alloy 780 shows very thin oxide layers but by far the biggest γ' depletion zone beneath the oxide scale. Note that for A718Plus after oxidation at 900 °C, no γ' is visible in the SEM and therefore no depletion zone is given.

To chemically analyze the different oxide layers, EDX mapping is shown in Figure 7. Due to no differences between oxidation in dry and humid atmosphere, only samples that were oxidized in humid atmosphere are shown. All samples that exhibit non-protective oxide scales demonstrate a homogeneous thick outer layer that is rich in Cr. Below this outer oxide scale, the Al-rich oxide penetrated into the sample. This fits well to examinations of the oxidation behavior of other commercial Ni-base superalloys. There, these layers were identified as Cr_2O_3 and Al_2O_3 accordingly.^[15,28] Between the Cr_2O_3 and Al_2O_3 scale, δ and η precipitates form in VDM Alloy 780 and A718Plus, which was also recently shown in literature for A718Plus.^[29,30] Compared to the other alloys, the Al_2O_3 layer in VDM Alloy 780 is continuous and more confined to the surface of the sample. This could most likely be attributed to an early growth of Al_2O_3 that is mainly facilitated by the higher Al content in VDM Alloy 780 compared to A718Plus. In case of Udimet 720Li, the Cr_2O_3 oxide layer is surrounded by a Ti-rich oxide layer which has been identified as TiO_2 in other studies^[28,31,32] and is only apparent in Udimet 720Li due to the significantly higher Ti content of the alloy compared to VDM Alloy 780 and A718Plus.

At 800 °C (Figures 7(a), (c), (e)), it is also visible that the Al_2O_3 oxide growth into the bulk material predominantly takes place at δ and η precipitate–matrix interfaces, indicated by red arrows, especially in VDM Alloy 780 and A718Plus. This effect seems to be less pronounced after oxidation at 900 °C. Here, VDM Alloy 780 shows nearly no internal Al_2O_3 below the protective layer while Al forms thick and connected internal oxides in A718Plus that reach into the bulk material. At this stage of oxidation, the internal oxides appear only slightly affected by the adjacent δ and η phases. In Udimet 720Li, primary γ' ^[33,34] does not seem

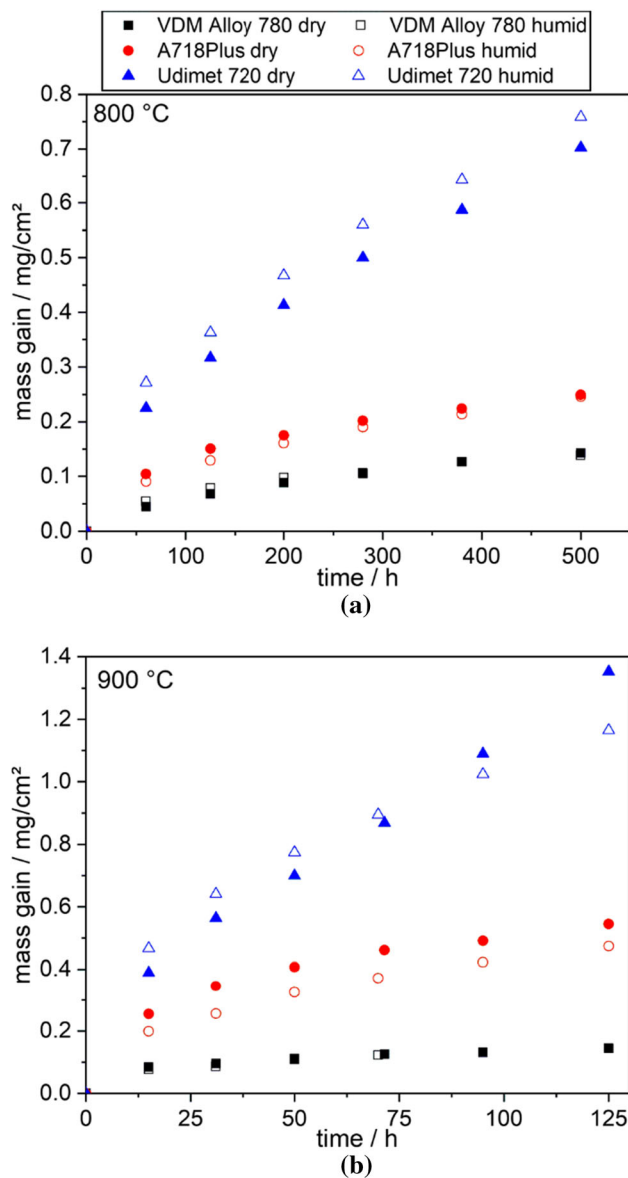


Fig. 4—Mass gain measurements at (a) 800 °C and (b) 900 °C in dry and humid atmosphere.

Table III. Parabolic Rate Constants in $10^{-3} \text{ mg}^2/\text{cm}^4 \text{ h}$

	800 °C Dry	800 °C Humid	900 °C Dry	900 °C Humid
VDM Alloy 780	0.04	0.04	0.15	0.15
A718Plus	0.12	0.12	2.28	1.77
Udimet 720Li	0.97	1.13	—	10.61

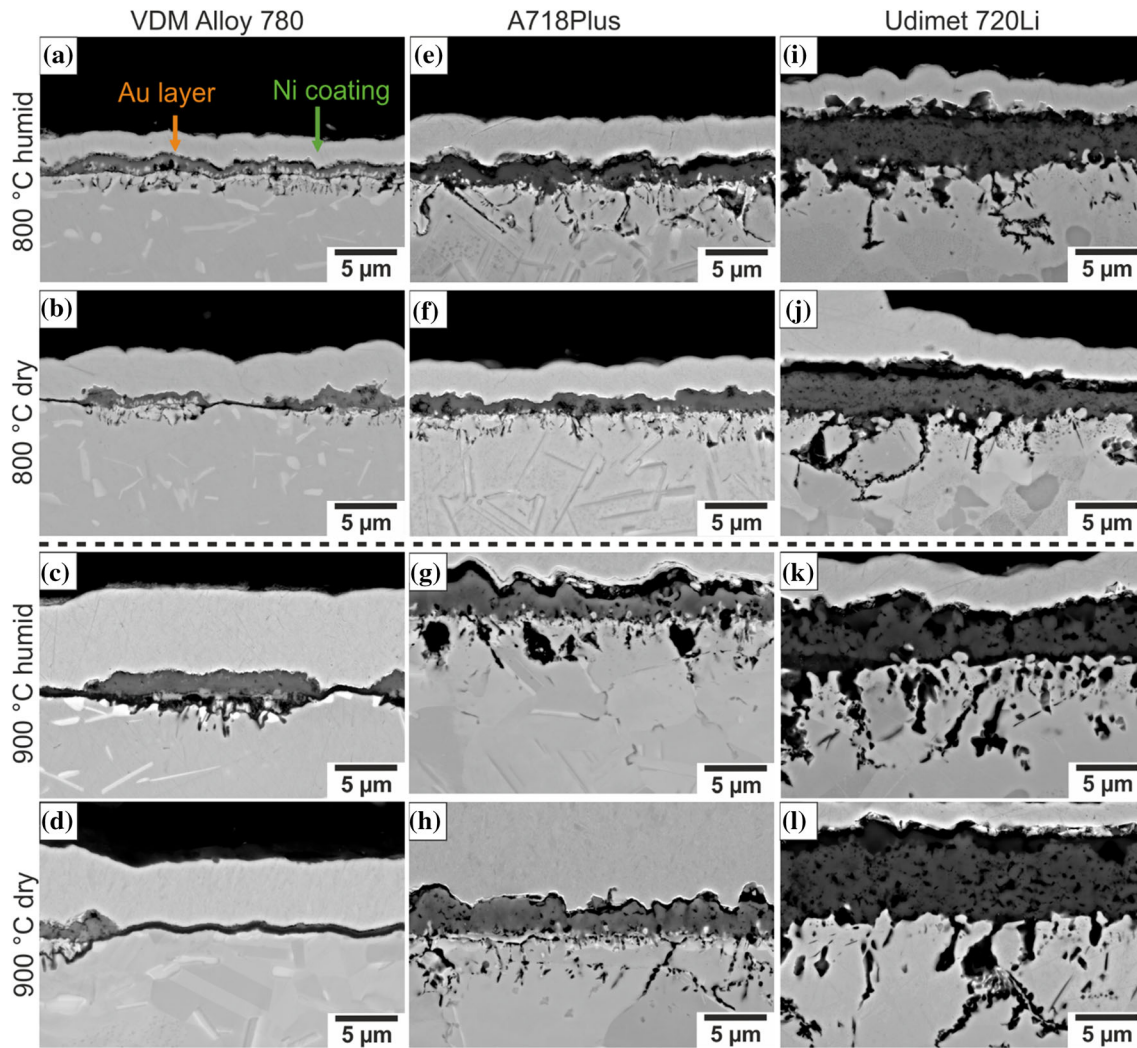


Fig. 5—BSD images of the oxide layers of (a) to (d) VDM Alloy 780, (e) to (h) A718Plus and Udimet 720, (i) to (l) after 500 h at 800 °C and 125 h at 900 °C in dry and humid air. A thin Au layer (orange arrow) to enhance the conductivity followed by a Ni coating (green arrow) protected the oxide scale during metallographic preparation (Color figure online).

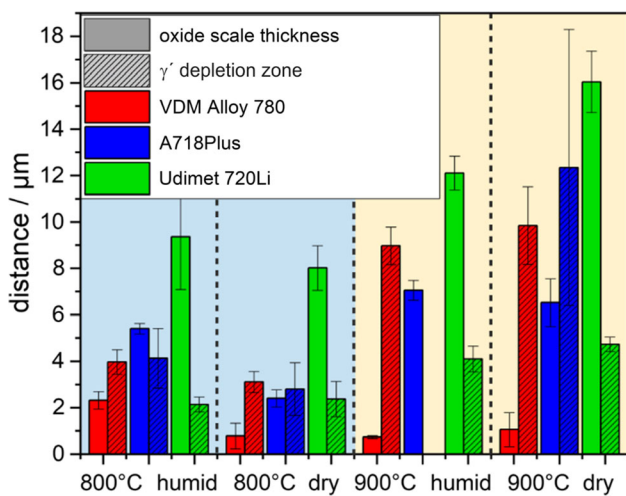


Fig. 6—Measured average thickness of oxide scales and γ' -depleted zones after oxidation for 500 h at 800 °C or 125 h at 900 °C in humid and dry atmosphere.

to have an influence on the development of Al_2O_3 after exposure to 900 °C.

To further analyze and distinguish the oxide layer in VDM Alloy 780, STEM analysis with corresponding STEM EDX and TEM EDX measurements were conducted (Figure 8). After exposure at 800 °C for 500 h (Figure 8(a)), a multiphase, continuous oxide layer with oxidation into the bulk material is visible. STEM EDX measurement (Figure 8(c)) shows that the main part of the top oxide layer is rich in Cr and therefore most likely Cr_2O_3 with a thickness of 827 nm. The dark phase can be distinguished in a Ni-rich phase with an average diameter of about 193 nm and a Ni and Nb-rich phase with an average diameter 236 nm. The bottom layer is Al-rich, therefore most likely Al_2O_3 . The bulk oxidation is significantly influenced by the Nb-rich δ and η precipitates as the Al_2O_3 is especially pronounced in the bulk material around these precipitates. When no δ or η are adjacent to the oxide layer, a thin-bottom Al_2O_3 layer is formed with no oxidation in the bulk material.

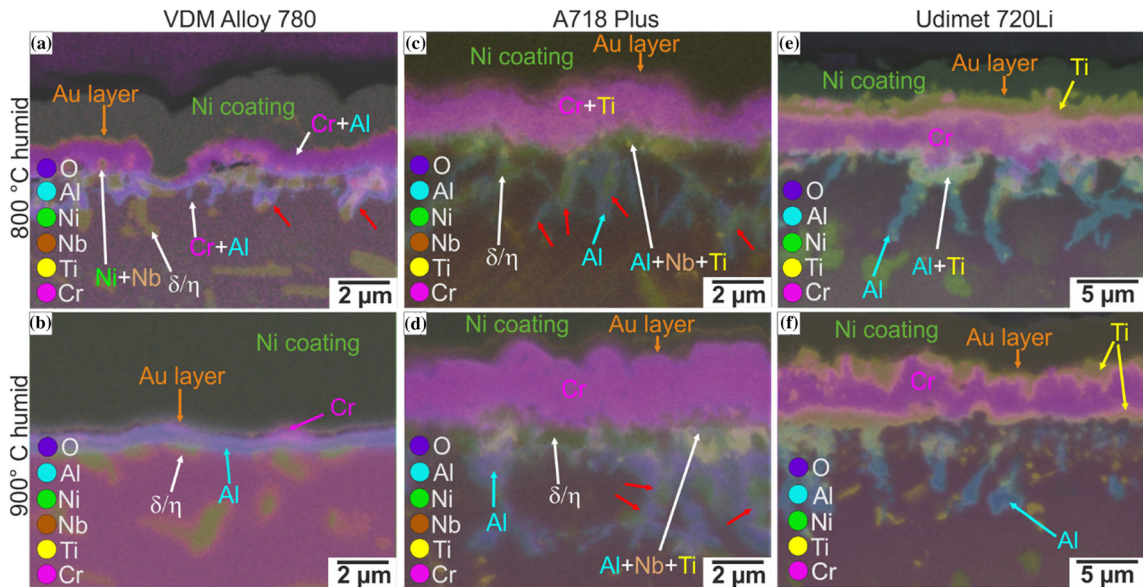


Fig. 7—EDX elemental distribution maps of (a), (b) VDM Alloy 780, (c), (d) A718Plus, and (e), (f) Udimet 720Li after 800 °C for 500 h and 900 °C for 125 h in humid atmosphere. The red arrows indicate oxidation along the δ/η -matrix interface (Color figure online).

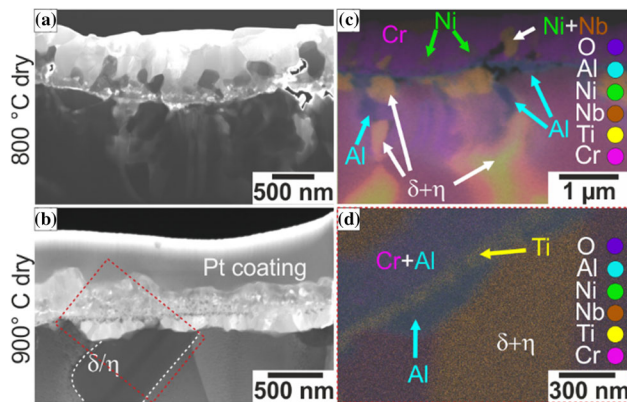


Fig. 8—Oxide layer of VDM Alloy 780 after (a), (c) 800 °C for 500 h and (b), (d) 900 °C for 125 h in dry atmosphere: (a), (b) STEM bright field images, (c) STEM EDX mapping of the area shown in (a) and (d) TEM EDX measurement of the area indicated by the red rectangle in (b) (Color figure online).

After oxidation at 900 °C for 125 h (Figure 8(b)), two layers separated by a thin layer can be distinguished. The elemental distribution (Figure 8(d)) demonstrated a comparably homogeneous Cr- and Al-rich oxide as top layer and an Al-rich oxide as bottom layer. These two layers are separated by a Ti-rich oxide layer. With these new insights, one can state that the inner layer is presumably Al_2O_3 with a thickness of 155 nm, the top layer is most likely Cr_2O_3 with a measured thickness of 255 nm and the layer in between presumably is TiO_2 with a thickness of 77 nm. While the Cr_2O_3 layer still exhibits a certain degree of porosity, no pores can be seen in the Al_2O_3 in the displayed area. Furthermore, it seems that neither of the two oxide layers is in any kind affected by the adjacent δ/η phase. Increased material

transport along interfaces appears to have only a minor effect on the growth of oxide scales on VDM Alloy 780 after 125 h at 900 °C.

IV. DISCUSSION

The mass gain results depicted in Figure 4 and the parabolic rate constants in Table III show that the two different atmospheres used in this work seem to have no impact on the oxidation behavior of VDM Alloy 780, in contrast to A718Plus and Udimet 720Li. However, this difference did not result in a microstructural change of the oxide layers in dry and humid atmosphere expect a change in the oxide layer thickness as seen in Figure 5. The oxidation behavior of chromia-forming Ni-base alloys was reported to be widely independent from water content in the test gas by Schieck *et al.*^[35] This is contrary to the results from Zurek *et al.*^[36] there the presence of water vapor lead to a considerable faster growth rate of Cr_2O_3 in a Ni-Cr model alloy due to a faster oxygen diffusion at oxide grain boundaries and restricted grain boundary movement due to interaction of adsorbed H_2O . An explanation for this contradicting results can be derived from studies by Kruk *et al.*^[30] They showed that at shorter oxidation times (45 h) of A718Plus at 850 °C the mass gain in humid atmosphere was smaller compared to that in dry atmosphere. After 650 h, however, this behavior was inverted and the mass gain and oxide scale thickness in humid atmosphere were significantly bigger compared to that in dry atmosphere. Comparing these results to Figures 4 and 6, the assumption can be made that longer oxidation times than used in this study could also lead to a higher oxidation rate in humid atmosphere compared to dry atmosphere.

In general, the formation of a protective oxide layer relies on a sufficiently fast transport of solute elements to the oxidation front.^[37,38] This means a sufficient supply of Cr and Al for an early formation of continuous protective Cr₂O₃ and Al₂O₃ layers is needed. An indirect measure for the depth of Al depletion is the evaluation of γ' -depleted regions below the oxide scale (Figure 6). It is well known that the γ' phase dissolves when the Al concentration falls below a certain level.^[36,37] For both considered temperatures, the novel VDM Alloy 780 demonstrates wider γ' -depleted zones and therefore also deeper depletion in Al. This indicates an increased mobility of Al in VDM Alloy 780 compared to conventional Udimet 720Li. This could be also facilitated by the slightly smaller grain size of VDM Alloy 780 compared to A718Plus and Udimet 720Li although the differences in grain sizes are minor. Additionally, higher temperatures reduce the formation of internal Al₂O₃, as the needed Al can diffuse faster to the surface of the sample. This is the case for VDM Alloy 780, especially after oxidation at 900 °C for 125 h, as both specimens mainly indicate thin and homogenous layers. The outward growth of Cr-rich oxide that is accompanied by internal formation of discrete Al₂O₃ only appears in isolated regions. What distinguishes the VDM Alloy 780 from the other tested samples might be the higher Al/Ti ratio (at. pct) of 12.6 in comparison with the Al/Ti ratio of A718Plus (3.4) and Udimet 720Li (0.9) calculated from the average nominal composition. Consequently, no Ti-rich layer is visible in VDM Alloy 780 after oxidation at 800 °C (Figures 7(a) and 8(c)) and only a few nanometer thin TiO₂ layer has formed after 900 °C, as seen in Figure 8(d). In contrast, in A718Plus, a Ti enrichment is present close to the Al₂O₃ layer (Figures 7(c, d)) as well as inside the Cr-oxide layer (Figure 7(c)). Investigations by Lech *et al.* revealed that Ti-rich oxide particles formed within the chromia scale in A718Plus,^[29] which explains also the found Ti enrichment in this study. In Udimet 720Li, the effect of Ti is even more pronounced. The outer oxide scale interface is a thick TiO₂ layer above the Cr₂O₃ layer which is followed by a second TiO₂ layer between the Cr₂O₃ and the Al₂O₃ (Figures 7(e) and (f)). The growth of transition oxides in Ni-base alloys was postulated to take place during the early stages of oxidation. However, after detailed APT investigation, also the diffusional transport of Ti through Cr-rich oxides appears possible,^[39] which could explain the two TiO₂ layers in Udimet 720Li. Correlating these microstructural results to the detected mass gain and the oxide layer thickness shown in Figures 4 and 6, respectively, it appears that the higher Al/Ti of VDM Alloy 780 promotes the oxidation resistance.

The effect of Ti as alloying element on the growth of Cr-rich oxide layers in Ni-base alloys was already elucidated in several publications. Ti was reported to increase the growth rate of chromia scales on Ni-base alloys.^[31,40] Especially the formation of TiO₂ in Udimet 720Li and the associated high weight gain^[31] is a well-known drawback of the respective alloy in the investigated temperature regime (750 °C to 1000 °C). Similar oxide scale morphologies were found for further

commercial Ni-base alloys with Ti as minor alloying element.^[28,41,42] The growth of oxide phases enriched in both, Al and Ti, as seen in Figure 7(c) was also reported for model cast Ni-base superalloys.^[42] However, the significantly higher Ti enrichment in the oxide scales of A718Plus is intriguing. Electron micrographs demonstrate a depletion of γ' below the oxide scale in all specimens. Additionally, the displayed micrographs after oxidation at 800 °C (Figures 5(e) and (f)) demonstrate a significant number of δ and η precipitates in the grains. Shorter oxidation at 900 °C leads to dissolution of these δ and η phases below the internal oxidation front from the inner-grain region but not from the grain boundaries in A718Plus (Figures 5(g) and (h)). This might act as a reservoir for Ti in regions that are adjacent to the alloy/scale interface during oxidation. This finding can lead to the conclusion that the higher stability of grain boundary precipitates in VDM Alloy 780 contribute to the improved resistance against oxide growth.

Additionally, the addition of Al in more complex multiphase superalloys was demonstrated to mostly prevent the early transition to breakaway oxidation,^[35,42,43] a mechanism where the formation of Cr₂O₃ leads to a Cr depleted zone. Then the Cr₂O₃ layer breaks due to mechanical or chemical failure, and no new Cr₂O₃ is able to form, which leads to a formation of unfavorable spinel oxides.^[44] This could be the case in A718Plus, which could explain the Ti-rich precipitates close to the oxide layer, while no noteworthy Cr depletion is visible in VDM Alloy 780 and Udimet 720Li. However, the negative effect of a high Ti content seems to outweigh the positive effect of a high Al content, as VDM Alloy 780 has a lower Al content compared to Udimet 720Li but performs significantly better. Additionally, VDM Alloy 780 forms a solid and homogenous Al₂O₃ layer, especially after oxidation at 900 °C. As stated above, this diffusion barrier can significantly reduce further oxidation and is therefore desired to guarantee the resistance/endurance of the Ni-base alloy during service.

The δ and η precipitates lead to a faster diffusion of oxygen due to additional phase–matrix interfaces and therefore stronger oxidation along precipitate boundaries.^[45,46] Additionally, the Al-containing δ and η phase can locally act as Al reservoir. Furthermore, VDM Alloy 780 has less and more blocky δ and η precipitates, compared to the elongated δ and η precipitates of A718Plus. Consequently, less interfaces are present and therefore less oxygen transport is possible, which leads to a less pronounced growth of Al₂O₃ in the bulk material. The reason why the δ and η precipitates in VDM Alloy 780 show no effect on the oxide layer after oxidation at 900 °C could not be clarified in this study; however, it can be assumed that a combination of the higher temperature and the high Al/Ti ratio is responsible for this phenomena.

V. SUMMARY AND CONCLUSION

In this study, the microstructure and the oxidation properties of the new Ni-base superalloy VDM Alloy 780 together with A718Plus and Udimet 720Li were

analyzed. The microstructural investigation showed that the δ and η phase precipitate either beside each other in blocky precipitates or inside each other in a fine lamellar structure. APT measurements revealed the chemical composition of the Al- and Nb-rich secondary precipitates which are embedded in a medium entropy CoNiCr-like γ matrix phase with similar concentrations of Ni, Co, and Cr. The new Ni-base superalloy VDM Alloy 780 shows superior oxidation resistance compared to commercially used Ni-base superalloys A718Plus and Udimet 720Li. Especially at 900 °C, the growth of a continuous, homogenous Al₂O₃ oxide layer is responsible for the improved oxidation behavior. STEM investigation on these oxide layers shows a thin and solid Al₂O₃ with no oxidation into the bulk material and a small TiO₂ layer. The higher Al/Ti ratio of VDM Alloy 780 compared to A718Plus and Udimet 720Li seems to have a significant positive influence on the oxidation resistance of the alloy. No significant influence of the δ and η precipitates in VDM Alloy 780 after oxidation at 900 °C could be revealed in contrast to the other specimens. VDM Alloy 780 shows oxide layers of less than 2 μ m thickness after 800 °C for 500 h and less than 1 μ m thickness after 900 °C for 125 h. In contrast, the commercially used Ni-base superalloys tested in this study show oxide thicknesses in the range of 2 μ m to 7 μ m for A718Plus and 8 to 16 μ m for Udimet 720Li after 800 °C for 500 h and after 900 °C for 125 h accordingly.

ACKNOWLEDGMENTS

This work was conducted as part of collaboration between Friedrich-Alexander-Universität Erlangen-Nürnberg (FAU) and VDM Metals International. The authors would like to thank Rolls Royce Germany for providing the testing materials A718Plus and Udimet 720Li.

FUNDING

Open Access funding enabled and organized by Projekt DEAL.

CONFLICT OF INTEREST

On behalf of all authors, the corresponding author states that there is no conflict of interest.

OPEN ACCESS

This article is licensed under a Creative Commons Attribution 4.0 International License, which permits use, sharing, adaptation, distribution and reproduction in any medium or format, as long as you give appropriate credit to the original author(s) and the source, provide a link to the Creative Commons licence, and indicate if changes were made. The images or other

third party material in this article are included in the article's Creative Commons licence, unless indicated otherwise in a credit line to the material. If material is not included in the article's Creative Commons licence and your intended use is not permitted by statutory regulation or exceeds the permitted use, you will need to obtain permission directly from the copyright holder. To view a copy of this licence, visit <http://creativecommons.org/licenses/by/4.0/>.

REFERENCES

1. R.C. Reed: *The Superalloys: Fundamentals and Applications*, 1st ed. Cambridge University Press, New York, 2006.
2. K. Bohan, E.V. Klapdor, B. Prade, A. Haeggmark, B. Ghenadie, P. Nakul, M. Welch, P. Adamsson, and T. Johnke: *Hydrogen for Gas Turbines* (white paper, 2020) <https://www.infrastructureasia.org/-/media/Articles-for-ASIA-Panel/Siemens-Energy-Hydrogen-Power-with-Siemens-Gas-Turbines.ashx>. Accessed 11 January 2022.
3. J. Rösler, T. Hentrich, and B. Gehrman: *Metals*, 2019, vol. 9, pp. 1–20.
4. K. Löhnert and F. Pyczak: *7th International Symposium on Superalloy 718 and Derivates*, 2010.
5. O.M. Messé, J.S. Barnard, E.J. Pickering, P.A. Midgley, and C.M.F. Rae: *Philos. Mag.*, 2014, vol. 94, pp. 1132–52.
6. M. Bergner, J. Rösler, B. Gehrman, and J. Klöwer: *Proceedings of the 9th International Symposium on Superalloy 718 & Derivates: Energy, Aerospace, and Industrial Applications*, 2018, pp. 489–99.
7. D. Hausmann, A. Förner, M. Pröbstle, D. Hünert, P. Felfer, M. Göken, and S. Neumeier: *Advanced Engineering Materials*, 2021, p. 2100558.
8. F. Kümmel, A. Kirchmayer, C. Solís, M. Hofmann, S. Neumeier, and R. Gilles: *Metals*, 2021, vol. 11, p. 719.
9. C. Ghica, C. Solís, J. Munke, A. Stark, B. Gehrman, M. Bergner, J. Rösler, and R. Gilles: *J. Alloy Compd.*, 2020, vol. 814, p. 152157.
10. T. Fedorova, J. Rösler, J. Klöwer, and B. Gehrman: *MATEC Web Conf.*, 2014, vol. 14, p. 01003.
11. T. Fedorova, J. Rösler, B. Gehrman, and J. Klöwer: n.d., p. 11.
12. E.J. Pickering, H. Mathur, A. Bhowmik, O.M.D.M. Messé, J.S. Barnard, M.C. Hardy, R. Krakow, K. Loehnert, H.J. Stone, and C.M.F. Rae: *Acta Mater.*, 2012, vol. 60, pp. 2757–69.
13. S. Lech, A. Gil, G. Cempura, A. Agüero, A. Kruk, and A. Czyska-Filemonowicz: *Int. J. Mater. Res.*, 2019, vol. 110, pp. 42–48.
14. M.H. Li, X.F. Sun, J.G. Li, Z.Y. Zhang, T. Jin, H.R. Guan, and Z.Q. Hu: *Oxid. Met.*, 2003, vol. 59, pp. 591–605.
15. A. Sato, Y.-L. Chiu, and R.C. Reed: *Acta Mater.*, 2011, vol. 59, pp. 225–40.
16. C.S. Giggins and F.S. Pettit: *J. Electrochem. Soc.*, 1971, vol. 118, p. 1782–90.
17. F.H. Stott: *Rep. Prog. Phys.*, 1987, vol. 50, pp. 861–913.
18. F.S. Pettit: *Trans. Metall. Soc. AIME*, 1967, vol. 239, pp. 1297–1305.
19. VDM Metals International GmbH, VDM Powder 780 (*Vdm Metals*, 2020), https://www.vdm-metals.com/fileadmin/user_upload/Downloads/Data_Sheets/Data_Sheet_VDM_Powder_780.pdf. Accessed 12 June 2022.
20. ATI Allvac, A718Plus data sheet (*Atimaterials*, 2010) https://www.atimaterials.com/Products/Documents/datasheets/nickel-cobalt/nickel-based/ati_718plus_tds_en_v3.pdf. Accessed 12 June 2022.
21. Special metals: Product Handbook of high-performance nickel alloy (*special metals*) <https://www.specialmetals.com/documents/nickel-alloy-handbook.pdf>. Accessed 12 June 2022.
22. K. Thompson, D. Lawrence, D.J. Larson, J.D. Olson, T.F. Kelly, and B. Gorman: *Ultramicroscopy*, 2007, vol. 107, pp. 131–39.
23. A. Devaraj, D.E. Perea, J. Liu, L.M. Gordon, T.J. Prosa, P. Parikh, D.R. Diercks, S. Meher, R.P. Kollit, Y.S. Meng, and S. Thevuthasan: *Int. Mater. Rev.*, 2018, vol. 63, pp. 68–101.

24. C.A. Schneider, W.S. Rasband, and K.W. Eliceiri: *Nat. Methods*, 2012, vol. 9, pp. 671–75.
25. C. Solís, J. Munke, M. Bergner, A. Kriele, M.J. Mühlbauer, D.V. Cheptiakov, B. Gehrman, J. Rösler, and R. Gilles: *Metall. Mater. Trans. A*, 2018, vol. 49A, pp. 4373–81.
26. L. Viskari and K. Stiller: *Ultramicroscopy*, 2011, vol. 111, pp. 652–58.
27. C.E. Slone, J. Miao, E.P. George, and M.J. Mills: *Acta Mater.*, 2019, vol. 165, pp. 496–507.
28. S. Cruchley, H.E. Evans, M.P. Taylor, M.C. Hardy, and S. Stekovic: *Corros. Sci.*, 2013, vol. 75, pp. 58–66.
29. S. Lech, A. Kruk, A. Gil, G. Cempura, A. Agüero, and A. Czyska-Filemonowicz: *Scripta Mater.*, 2019, vol. 167, pp. 16–20.
30. A. Kruk, A. Gil, S. Lech, G. Cempura, A. Agüero, and A. Czyska-Filemonowicz: *Materials*, 2021, vol. 14, p. 6327.
31. J.H. Chen, P.M. Rogers, and J.A. Little: *Oxid. Met.*, 1997, vol. 47, pp. 381–410.
32. A.A.N. Németh, D.J. Crudden, D.E.J. Armstrong, D.M. Collins, K. Li, A.J. Wilkinson, C.R.M. Grovenor, and R.C. Reed: *Acta Mater.*, 2017, vol. 126, pp. 361–71.
33. R.C. Reed, M.P. Jackson, and Y.S. Na: *Metall. Mater. Trans. A*, 1999, vol. 30A, pp. 521–33.
34. M.P. Jackson and R.C. Reed: *Mater. Sci. Eng. A*, 1999, vol. 259, pp. 85–97.
35. M. Schiek, L. Niewolak, W. Nowak, G.H. Meier, R. Vaßen, and W.J. Quadackers: *Oxid. Met.*, 2015, vol. 84, pp. 661–94.
36. J. Zurek, D.J. Young, E. Essuman, M. Hänsel, H.J. Penkalla, L. Niewolak, and W.J. Quadackers: *Mater. Sci. Eng. A*, 2008, vol. 477, pp. 259–70.
37. M. Bensch, A. Sato, N. Warnken, E. Affeldt, R.C. Reed, and U. Glatzel: *Acta Mater.*, 2012, vol. 60, pp. 5468–80.
38. W. Zhao, Y. Kang, J.M.A. Orozco, and B. Gleeson: *Oxid. Met.*, 2015, vol. 83, pp. 187–201.
39. T.L. Barth and E.A. Marquis: *Oxid. Met.*, 2019, vol. 92, pp. 13–26.
40. H. Nagai and M. Okabayashi: *Trans. JIM*, 1981, vol. 22, pp. 691–98.
41. W.J. Nowak, B. Wierzba, and J. Sieniawski: *High Temp. Mater. Process.*, 2018, vol. 37, pp. 801–06.
42. K. Wollgarten, T. Galiullin, W.J. Nowak, W.J. Quadackers, and D. Naumenko: *Corros. Sci.*, 2020, vol. 173, p. 108774.
43. K.A. Unocic and B.A. Pint: *8th International Symposium on Superalloy 718 and Derivatives*, 2014, pp. 667–77.
44. T. Gheno, D. Monceau, and D.J. Young: *Corros. Sci.*, 2012, vol. 64, pp.222–33.
45. M. Sundararaman, P. Mukhopadhyay, and S. Banerjee: *MTA*, 1988, vol. 19, pp. 453–65.
46. A. Stratulat, D.E.J. Armstrong, and S.G. Roberts: *Corros. Sci.*, 2016, vol. 104, pp. 9–16.

Publisher's Note Springer Nature remains neutral with regard to jurisdictional claims in published maps and institutional affiliations.